Extreme Materials 2 (2026) 1–11

Contents lists available at ScienceDirect

Extreme Materials

journal homepage: www.keaipublishing.com/en/journals/extreme-materials/

Role of rare earth oxide modification in strengthening ZrB_2-SiC composites against oxidation and cyclic ablation

Mengen Hu[a,b,1], Xian Dang[a,b,1], Chengwan Yang[a,b], Kewei Li[a,b], Hanwen Zhang[a,b], Zhen Wang[a], Shuxin Li[a], Yuebin Li[c], Xiaoye Hu[a,b], Yue Li[a,d], Abdumutolib Atakhanov[e], Zhulin Huang[a,b,*], Guowen Meng[a,b]

[a] Key Laboratory of Materials Physics and Anhui Key Laboratory of Nanomaterials and Nanotechnology, Institute of Solid State Physics, HFIPS, Chinese Academy of Sciences, Hefei 230031, China
[b] University of Science and Technology of China, Hefei 230026, China
[c] Hubei University, Wuhan 430062, China
[d] School of Physical Science and Technology, Tiangong University, Tianjin 300387, China
[e] Institute of Polymer Chemistry and Physics, Uzbekistan Academy of Sciences, Tashkent 100128, Uzbekistan

ARTICLE INFO

Keywords:
ZrB_2-SiC composites
Rare earth
Doping modification
Oxidation resistance
Ablation resistance

ABSTRACT

ZrB_2-20SiC (ZS20) composite and its derivatives doped with 5 vol% Sc_2O_3, Y_2O_3, and La_2O_3 were densified using hot press sintering to investigate the influence of rare earth oxides on their high temperature oxidation and ablation behavior. Isothermal oxidation testing at 1773 K indicate that rare earth oxides modification lowers activation energy and slightly accelerates weight gain during the initial phase. As oxidation progresses, the weight gain of ZS20 increases sharply. The sample doped with La_2O_3 (ZS20L5) exhibits the lowest oxidation weight gain, with a porosity of only 1.8 % after oxidation. Cyclic ablation tests at the middle-low temperature zones indicate that ZS20L5 exhibits the lowest linear and mass ablation rates. Thermodynamic analyses demonstrate that La_2O_3 preferentially reacts with SiO_2 to form $La_2Si_2O_7$, which demonstrates a more effective oxygen barrier property compared to $ZrSiO_4$. Additionally, La_2O_3 enhances the fluidity of the glass phase, effectively filling cracks, sealing pores, and blocking the penetration of oxygen.

1. Introduction

As advanced technologies like hypersonic vehicles, round-trip orbital vehicles, and reusable space launch systems continue to evolve rapidly, the requirements for thermal protection materials for extreme environments have reached unprecedented levels of stringency [1–3]. Ultra-high temperature ceramics (UHTCs) have emerged as core candidates for ensuring reliable performance in ultra-high temperature aerobic environments owing to their exceptional structural integrity and chemical stability above 3000 ˚C, including transition metal carbides, nitrides, and borides [4–6]. Typically, boride UHTCs become the preferred thermal protection materials because of their excellent thermal conductivity and the formation of boron oxide (B_2O_3) during oxidation, which is beneficial for oxidation resistance [7–12]. Among boride UHTCs, zirconium diboride (ZrB_2) is recognized as a particularly advantageous material for thermal protection architectures due to its high oxidation activation energy and relatively moderate density [13–15].

ZrB_2 is oxidized at high temperatures to form porous zirconium oxide (ZrO_2) and liquid B_2O_3. This liquid B_2O_3 can infiltrate the pores and block the diffusion of oxygen, which is highly beneficial to the high temperature oxidation resistance of ZrB_2. However, when the temperatures exceed 1400 ℃, B_2O_3 will volatilize rapidly and lead to a reduction in oxidation resistance [16–20]. A common strategy is to add silicon carbide (SiC), which oxidizes at high temperatures to generate silicon oxide (SiO_2) and B_2O_3 to form borosilicate, demonstrating excellent oxidation resistance at temperatures as high as 1600 ℃ [21–24]. Nevertheless, when the temperature exceeds 1650 ℃ or under low

* Corresponding author at: Key Laboratory of Materials Physics and Anhui Key Laboratory of Nanomaterials and Nanotechnology, Institute of Solid State Physics, HFIPS, Chinese Academy of Sciences, Hefei 230031, China.
E-mail address: zlhuang@issp.ac.cn (Z. Huang).
[1] These authors contributed equally to this work.

https://doi.org/10.1016/j.exm.2025.12.001
Received 3 November 2025; Received in revised form 17 December 2025; Accepted 17 December 2025
Available online 19 December 2025

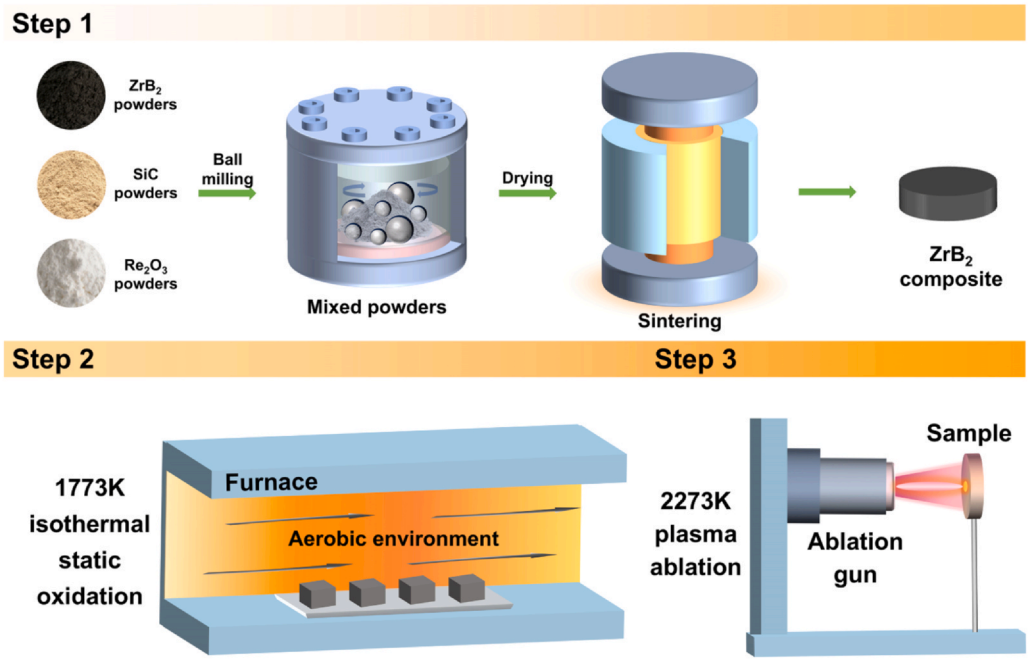

Fig. 1. Schematic drawing of the manufacturing procedure and performance evaluation of ZrB_2-SiC-based composites.

oxygen partial pressure condition, SiC will be oxidized to SiO. This effect is particularly pronounced when the temperature rises above 1800 ℃, triggering a marked reduction in material oxidation resistance [25–28]. To enhance the thermochemical durability of ZrB_2-SiC composites under extreme conditions, researchers have explored the modification of boride UHTCs with rare earth oxides. Specifically, the dissolution of rare earth oxides into borosilicate glass significantly not only alters its rheological properties but also exerts a pronounced effect on the oxidation resistance [29–31]. Lin et al. incorporated Y_2O_3 into ZrB_2-SiC composites to form a Zr-Si-Y-O glass layer at high temperature, which prevented oxygen diffusion and filled cracks to improve the oxidation resistance of the coating [32]. Hu et al. found that the addition of La_2O_3 in WB_2-SiC composites significantly improved their high-temperature ablation resistance due to the formation of rare earth borosilicates [33]. Qian et al. added La_2O_3 to HfB_2-SiC composites, which resulted in the formation of a multiphase glass layer of Hf-B-La-Si-O at high temperatures and significantly improved the oxidation resistance [34].

Numerous studies have demonstrated that incorporating rare earth oxides enhances the oxidation and ablation resistance of materials. However, the selection of different rare earth oxides and their mechanisms of action during elevated temperature oxidation and ablation process still need to be systematically investigated. This is essential to achieve the targeted design and property optimization of materials. Previous studies have shown that the ionic radii of rare earth elements influence the stability of SiO_2 at high temperatures. Additionally, Y_2O_3 has been shown to effectively stabilize ZrO_2 by inhibiting its phase transformation. It has also demonstrated higher adsorption energy and more negative solution energy in interaction with SiO_2 [35,36]. Among various rare earth oxides, La_2O_3 exhibits the most negative reaction free energy in forming rare earth silicates with SiO_2, indicating a greater propensity to form rare earth silicate at high temperatures [37]. Therefore, based on the ionic radius gradient design and ZrO_2, SiO_2 oxidation products, Sc_2O_3, Y_2O_3 and La_2O_3 were selected as modifiers. The differences in their ionic radii are expected to yield notably distinct modification effects in the ZrB_2-SiC system, providing an ideal basis for comparative studies to elucidate the action mechanisms of rare earth oxides.

In this study, composites of ZrB_2-20SiC (ZS20), ZrB_2-20SiC-5Sc_2O_3 (ZS20S5), ZrB_2-20SiC-5Y_2O_3 (ZS20Y5), and ZrB_2-20SiC-5La_2O_3 (ZS20L5) were synthesized by hot press sintering. Their microstructure evolution, oxidation kinetics at elevated temperatures, ablation resistance and failure mechanisms of ZrB_2-SiC composites were systematically investigated by integrating static oxidation (1773 K) and cyclic ablation tests at the middle-low temperature zones. In addition, the mechanism underlying the behavior for different additives at high temperatures was explored by employing a combination of multiscale characterization and simulation. This work aims to reveal the influence mechanisms of three rare earth oxides on glass phase rheology, oxygen barrier performance, and defect healing capability. It ultimately seeks to establish a composition-structure-property relationship model to facilitate the targeted design of UHTCs.

2. Materials and experimental methods

2.1. Materials

For the preparation of ZrB_2-SiC composites, the raw materials included silicon carbide (SiC, 99.9 % purity, D_{50} = 1.35 μm), scandium oxide (Sc_2O_3, 99.9 % purity, D_{50} = 13.5 μm), yttrium oxide (Y_2O_3, 99.9 % purity, D_{50} = 5.70 μm) and lanthanum oxide (La_2O_3, 99.9 % purity, D_{50} = 4.64 μm). All materials were purchased from Shanghai Aladdin Biochemical Technology Co., Ltd. The particle sizes and morphologies of SiC, Sc_2O_3, Y_2O_3 and La_2O_3 are presented in Fig. S1 and Fig. S2. The preparation of ZrB_2 powders was based on the previous research [38].

2.2. Fabrication of ZrB_2-SiC-based composites

The synthesis method of ZrB_2-SiC-based composites is illustrated in Step 1 of Fig. 1, primarily involving powder mixing and sintering process. In particular, an appropriate amount of ZrB_2, 20 vol% SiC and 5 vol% rare earth oxides powders were loaded into a ball milling jar. The 5 vol% rare earth oxide doping concentration was selected based on previous studies [39,40]. Using ZrO_2 balls and anhydrous ethanol as the grinding media, the mixture was ball-milled at 300 rpm for 6 h. Subsequently, the mixtures underwent solvent removal at 55 ℃ for 10 h, and then the dried mixture was ground in an agate mortar for 30 min to obtain homogeneous mixed powders. The mixed powders were

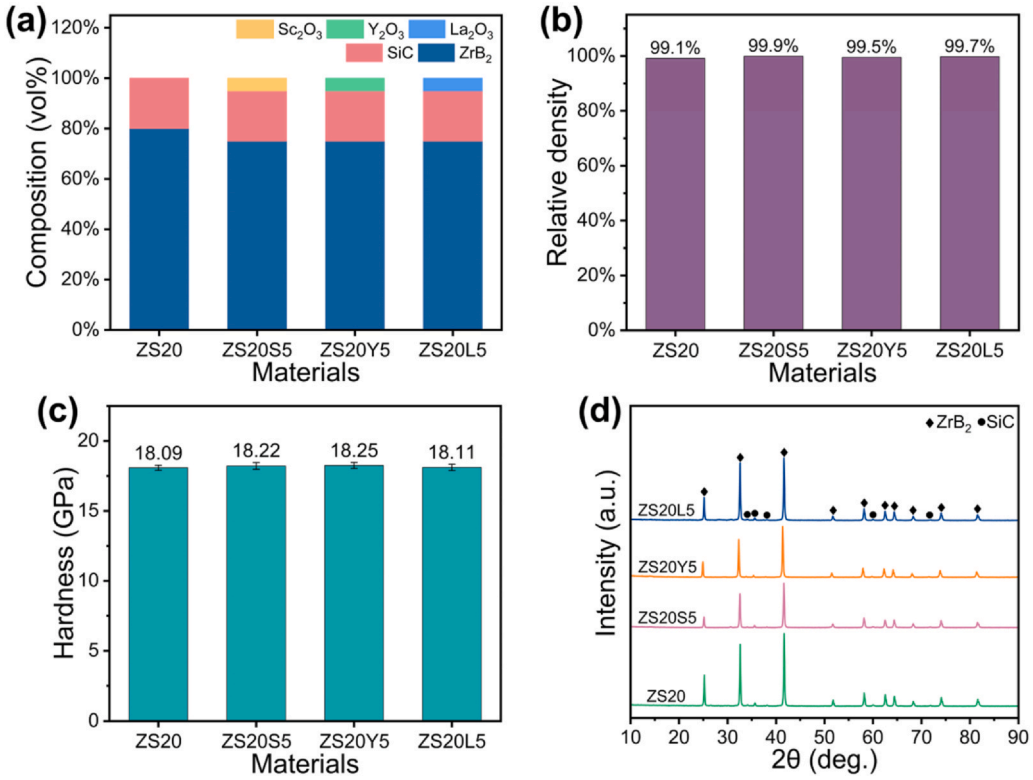

Fig. 2. Composition and physical properties of the samples: (a) component weight fraction of the composites, (b) relative density of the sintered samples, (c) Vickers hardness of the sintered samples, (d) XRD patterns of the sintered samples.

transferred to graphite mold and densified at 1800 ˚C for 2 h under 30 MPa. Upon completion, the load was removed and the furnace was cooled to ambient temperature. The bulk density was measured by the Archimedes drainage method, and the porosity was calculated based on the measured density [41].

2.3. Oxidation test

The hot-pressed samples were cut into 4 mm × 4 mm × 3 mm blocks, subsequently polished with sandpaper, and then ultrasonically cleaned in ethanol. The isothermal static oxidation test was performed as shown in step 2 of Fig. 1, conducted in a high temperature tube furnace at 1773 K (Hefei Kejing Material Technology Co. Ltd) in air. The samples were taken out every 10 min to cool down and be weighed, then returned for further oxidation. The SEM cross-section method was employed to determine the oxide layer thickness, which involves observing the cross-section of oxidized samples to measure the thickness from the oxide layer to the matrix interface.

2.4. Ablation test

The ablation resistance was performed using a customized plasma platform (Multiplaz 3500 generator), as shown in step 3 of Fig. 1. The ablation samples had a diameter of 20 mm and a thickness is 5 mm. The movement of the sample during the ablation process was controlled by a mechanism consisting of a reciprocating motor and a connecting rod. Each full rotation of the motor drove the specimen to complete one back-and-forth horizontal movement, corresponding to one ablation cycle. The duration for which the specimen remained at the ablation end represented the single loading time. The plasma was operated at 6 A/160 V power parameters with H_2O. The pressure of the compressed air supplied at 0.4 MPa and the flow rate of 2 m^3/h. Both the plasma and airflow nozzles had an inner diameter of 2 mm, positioned at a distance of 10 mm from the specimen surface, with the generated jet directed perpendicular to the specimen surface. Throughout ablation, the temperature at the center of the specimen surface was measured using two infrared pyrometers: the Endurance E3ML (323 −1273 K, ± 0.3 % accuracy, 20 ms response time) and the E1RH (1273 −3473 K, ± 0.5 % accuracy, 10 ms response time). The ablation flame was maintained at 2273 K and each cycle was 20 s, with 5 cycles repeated. The ablation rate was quantified by the change in central thickness and mass after ablation, yielding the linear ablation rate (LAR) and mass ablation rate (MAR), calculated via the equations below:

$$LAR = \frac{l_0 - l_1}{t} \tag{1}$$

$$MAR = \frac{m_0 - m_1}{t} \tag{2}$$

where l_0, l_1 and m_0, m_1 denote the initial and final thicknesses and masses, respectively, with t representing the total ablation time.

2.5. Characterization

The phase analysis was performed via X-ray diffraction (XRD, X'Pert pro, PANalytical, Netherlands). The microstructure of ZrB_2-SiC composites was examined with a scanning electron microscope (SEM, SU8020, Hitachi, Japan) integrated with an energy dispersive spectroscopy (EDS), the operating voltage of EDS was 15 kV, with an acquisition time of ≥ 60 s and a dead time controlled within 20 %. The particle distribution was measured using a laser particle size analyzer (Mastersizer 3000, Malvern, UK). Raman spectroscopy testing was conducted on a confocal Raman microscope (inVia Reflex, Renishaw, UK) employing a 532 nm laser source. Vickers hardness (Hv) measurements of the samples were carried out with a sclerometer (Wilson, VH3100, Switzerland). For each test, a minimum of five indentations were made under a 4.9 N load and held for 15 s.

3. Results and discussion

3.1. Compositions and characterizations of ZrB_2-SiC-based composites

Hot press sintering was employed to fabricate ZrB_2-SiC-based composites, with the preparation process illustrated in step 1 of Fig. 1, and the constituent volume fractions are provided in Fig. 2a. The relative density of the sintered blocks is presented in Fig. 2b, demonstrating that all samples achieve high densification. At a sintering temperature of 1800 ˚C, although no macroscopic liquid phase forms in the ZrB_2-SiC system, a liquid-solid coexistence may occur. This two-phase region plays a crucial role in both sintering densification and oxidation resistance. Following the addition of rare earth oxides, these oxides react with impurities on the SiC surface during sintering to form a eutectic liquid phase with a lower melting point. This liquid phase may also accumulate B_2O_3 present on the surface of ZrB_2 particles, which can significantly enhance particle fluidity and diffusion coefficients during sintering, thereby promoting material densification and improving the overall density of the composites [39]. Fig. 2c displays the hardness comparisons before and after doping with rare earth oxides, indicating that incorporation of rare earth oxides preserved the mechanical integrity of the composites. XRD analysis of the sintered samples is presented in Fig. 2d. The primary phases are ZrB_2 and SiC, with no diffraction peaks of other substances detected. The attenuated SiC peak is attributed to the dominant ZrB_2 signal. In addition, the absence of rare earth oxides characteristic peaks may be due to the low doping concentration. The microstructure of the polished surface and cross-sections of the four samples are presented in Fig. 3. All specimens possess a high-density microstructure with no noticeable defects. The fracture surfaces of the composites reveal that the fracture mode is a mixture of intergranular and transgranular fractures. SEM and EDS mapping results indicate that SiC exhibits a relatively uniform distribution in the matrix (Fig. S3).

3.2. Oxidation behavior and mechanism of ZrB_2-SiC-based composites

The oxidation behavior of ZS20, ZS20S5, ZS20Y5, and ZS20L5 samples was investigated using isothermal oxidation at 1773 K. The isothermal static oxidation test is performed as shown in step 2 of Fig. 1. The dependence of weight gain on oxidation time is shown in Fig. 4a, b. As the oxidation time progressed, all four composites exhibited a continuous weight increase. In the initial 140 min, ZS20 exhibited comparatively slow oxidation weight gain, lower than that of ZS20S5, ZS20Y, and ZS20L5. The oxidation-induced weight gain of the four samples was analyzed at different temperatures (Fig. S4), and the activation energy for their initial oxidation stage was calculated using the Arrhenius equation [42]. The incorporation of rare earth oxides reduced the oxidation activation energy of the composites (Fig. S5), leading to accelerated oxidation kinetics for the doped specimens relative to ZS20 during the initial oxidation stage. The oxidation weight gain of ZS20 increased rapidly and soon exceeded that of the composites containing rare earth oxides after 140 min, indicating a significant decline in the oxidation resistance of ZS20 during prolonged high temperature exposure. In contrast, ZS20S5, ZS20Y5, and ZS20L5 samples maintained relatively stable oxidation weight gain, demonstrating excellent long-term oxidation resistance, with ZS20L5 exhibiting the

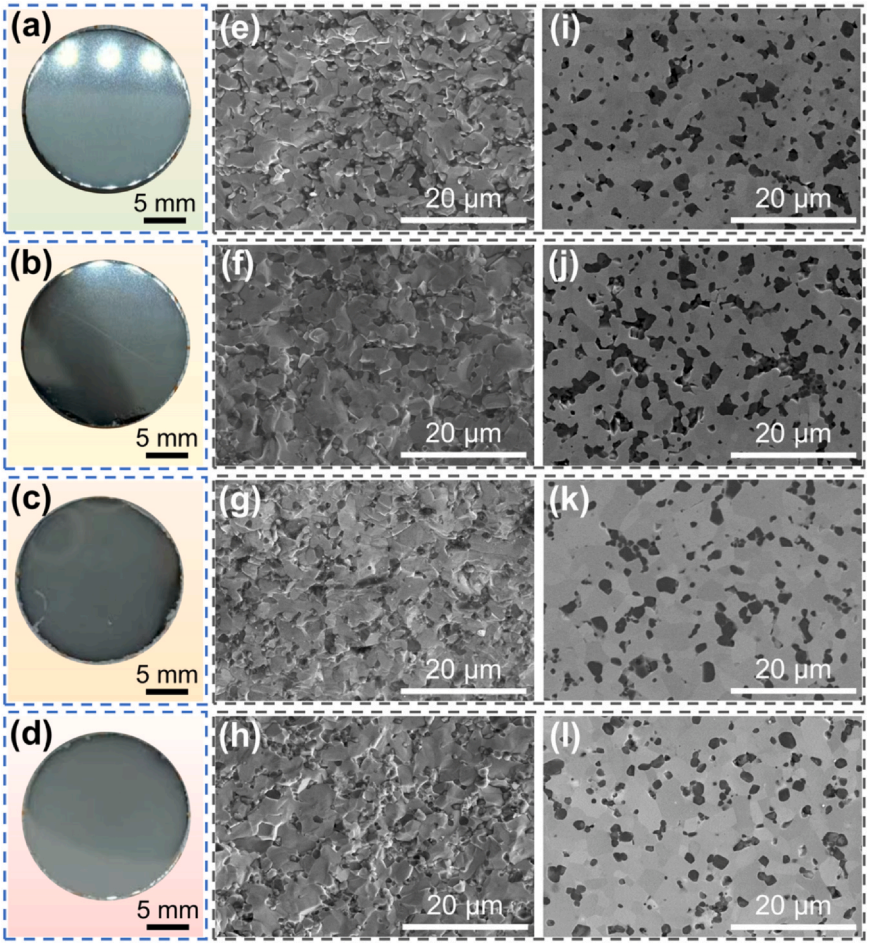

Fig. 3. Microstructural characterization of the sintered composites: (a-d) macrographs of ZS20, ZS20S5, ZS20Y5, and ZS20L5. SEM micrographs of (e-h) fracture surface and (i-l) polished surface.

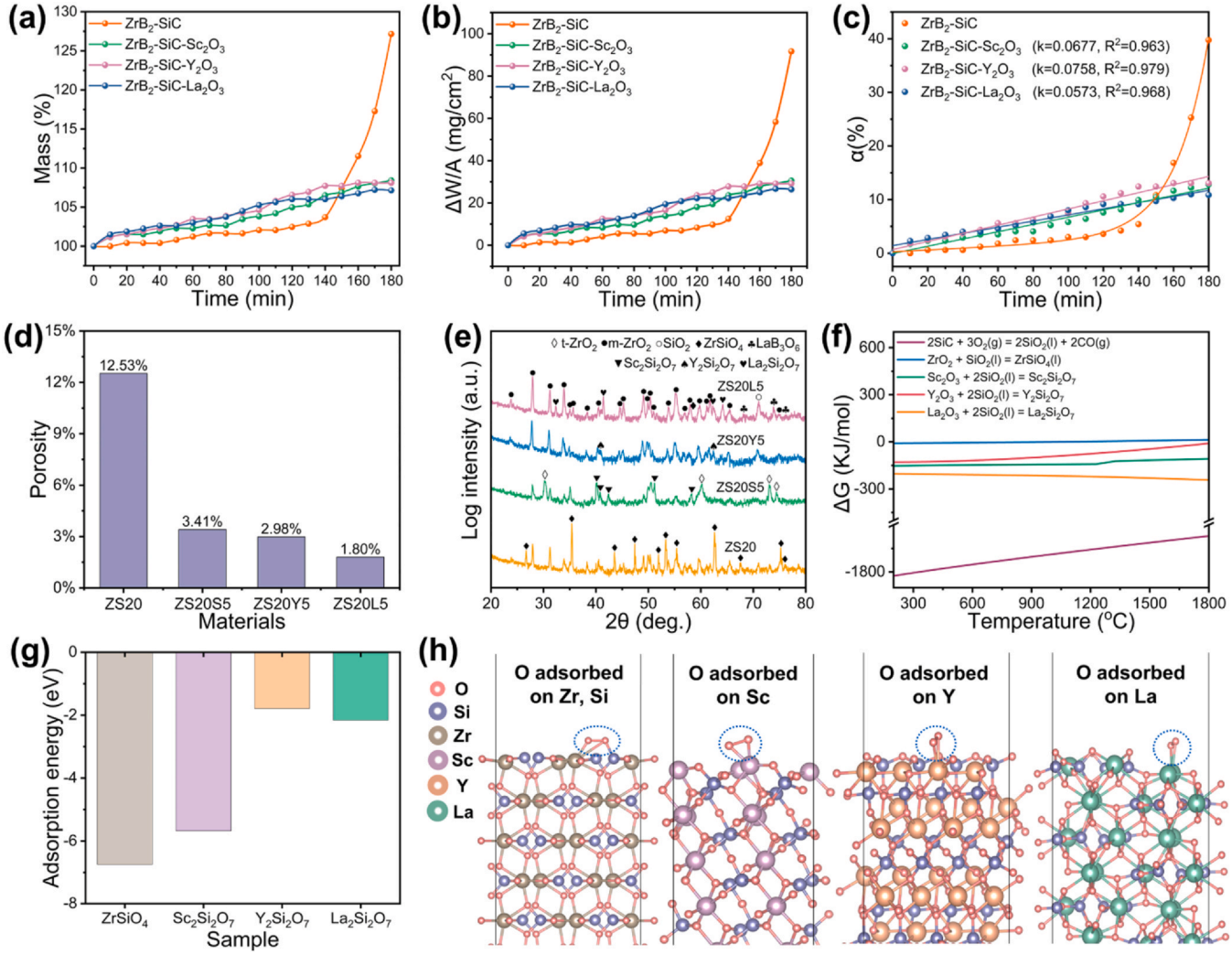

Fig. 4. Oxidation testing and mechanism of the fabricated composites at 1773 K: (a) oxidation weight changes of the samples, (b) plots of (ΔW/A) versus oxidation time of the samples, (c) α changes of the samples as a function of time during isothermal oxidation, (d) porosity of the samples after oxidation, (e) XRD patterns of the oxidized samples, (f) variation of standard reaction Gibbs free energy with temperature during the oxidation process, (g, h) absorption energy of oxygen on the metal sites of the rare earth silicates (001) surface calculated by DFT.

optimal performance. This was further confirmed by the fitted plot of $(\Delta W/A)^2$ versus oxidation time presented in Fig. S6.

Fig. 4c shows the oxidation kinetics of the four composites [43]. For the ZS20 sample, there was a linear relationship between the oxidation degree (α) and oxidation time at the initial stage. However, the oxidation degree increased rapidly in the later stages, indicating the failure of the oxidation protection layer. In contrast, the samples doped with rare earth oxides exhibited a linear relationship between α and oxidation time throughout the oxidation process, indicating that a relatively stable oxide barrier capable of effectively restricting oxygen ingress, resulting in a continuous oxidation at a constant rate. The oxidation rate constant (k) of ZS20S5, ZS20Y5, and ZS20L5 samples was calculated using the Jander equation [44], with the k value of ZS20L5 being 0.0573, indicating its superior oxidation resistance. Fig. 4d presents the porosities of the four composites after oxidation, revealing that the samples containing rare earth oxides were significantly less porous ZS20. Specifically, the porosity of ZS20L5 after oxidation was only 1.8 %, further confirming that La_2O_3 addition effectively improves the oxidation resistance of ZrB_2-SiC composite. This improvement is likely due to the better oxygen-blocking properties of the protective layer formed after the incorporation of La_2O_3. Fig. 4e demonstrates the XRD results of the oxidized composites. The main phases of ZS20 after oxidation are $ZrSiO_4$ and m-ZrO_2, while those of ZS20S5 are m-ZrO_2, t-ZrO_2, and $Sc_2Si_2O_7$, suggesting that Sc_2O_3 doping effectively suppresses the transformation of t-ZrO_2 to m-ZrO_2. For ZS20Y5, the primary oxidized phases are m-ZrO_2 and $Y_2Si_2O_7$, while the primary phases of ZS20L5 after oxidation are m-ZrO_2 and $La_2Si_2O_7$, with no detectable characteristic peaks of $ZrSiO_4$. The XRD patterns after oxidation clearly show the formation of $Sc_2Si_2O_7$, $Y_2Si_2O_7$, and $La_2Si_2O_7$. This can be attributed to the reaction between rare earth oxides and SiO_2 at high temperatures during the oxidation process, resulting in the synthesis of silicate phases with good crystallinity. The generated $Re_2Si_2O_7$ continuously accumulated in the oxide layer, exceeding the XRD detection limit. Moreover, ZrO_2 formed by ZrB_2 oxidation exhibits relatively poor crystallinity, resulting in peak intensity insufficient to mask the $Re_2Si_2O_7$ signal. The thermodynamics of the reactions involved in high temperature oxidation are shown in Fig. 4f. In the case of the ZS20 sample, ZrO_2 generated during high temperature oxidation reacts with SiO_2 to form $ZrSiO_4$, which is also thermodynamically favorable. For the ZS20S5, ZS20Y5 and ZS20L5 samples, the formation of rare earth silicates is thermodynamically favored, as evidenced by the more negative Gibbs free energy (ΔG) values for the reactions between rare earth oxides and SiO_2 at elevated temperatures. This thermodynamic preference aligns with the phase identification results from XRD (Fig. 4e).

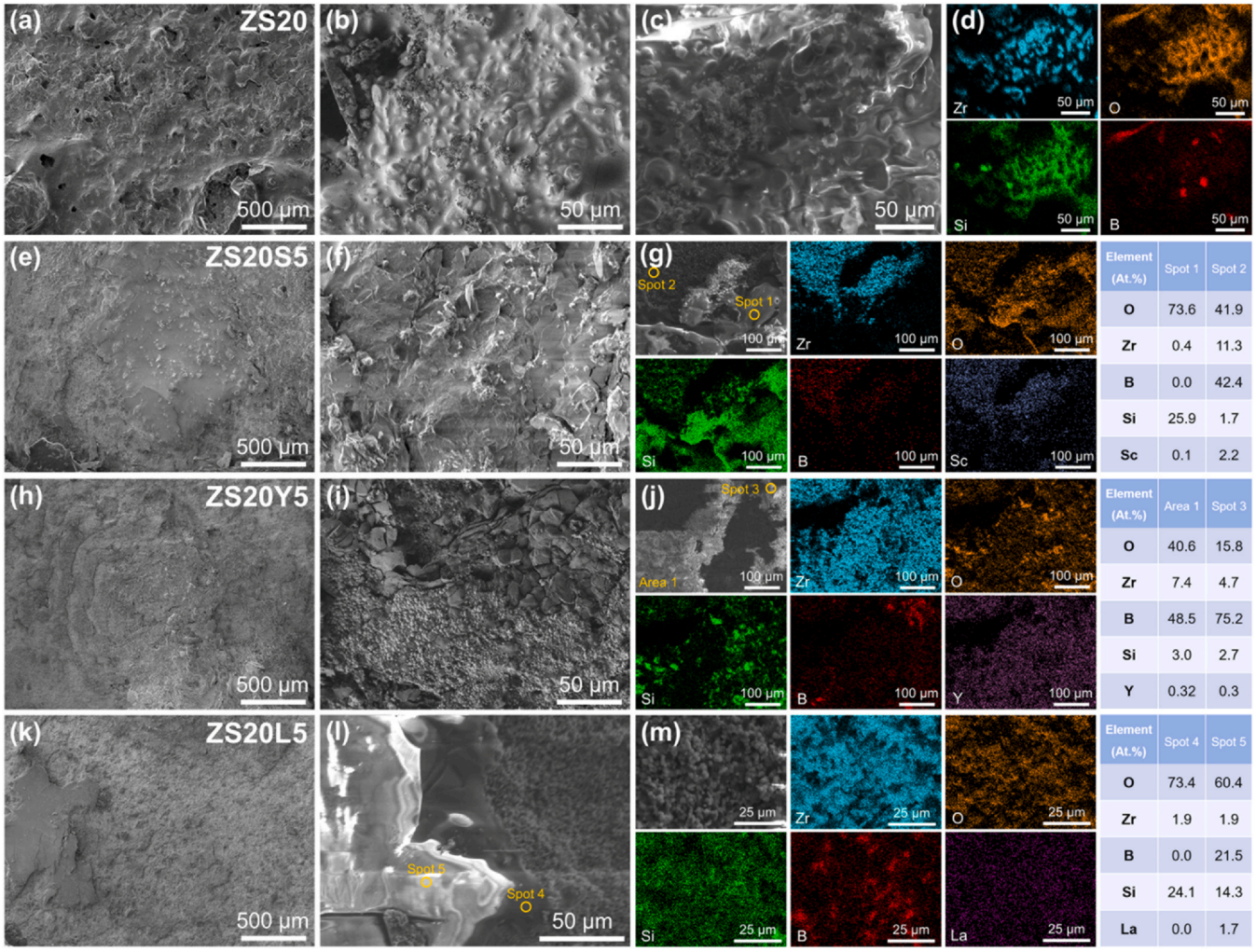

Fig. 5. SEM-EDS analysis of the oxidized surface of the composites oxidized at 1773 K for 180 min: (a-d) ZS20, (e-g) ZS20S5, (h-j) ZS20Y5, (k-m) ZS20L5.

To further reveal the mechanism by which the addition of rare earth oxides enhances oxidation resistance, density functional theory (DFT) was performed to calculate the oxygen adsorption energy at metal sites on the (001) surfaces of $ZrSiO_4$, $Sc_2Si_2O_7$, $Y_2Si_2O_7$, and $La_2Si_2O_7$. As shown in Fig. 4g, e, $ZrSiO_4$ exhibits the lowest oxygen adsorption energy, indicating a higher propensity for oxygen adsorption. Subsequently, $Sc_2Si_2O_7$, $La_2Si_2O_7$, and $Y_2Si_2O_7$ exhibit progressively higher adsorption energies, suggesting that the rare earth silicates formed after the addition rare earth oxide exhibit a stronger resistance to oxygen adsorption. Consequently, during the initial oxidation stage, the formation of ZrO_2 and SiO_2 is limited due to low oxidation degrees, resulting in minimal generation of $ZrSiO_4$. As oxidation time prolongs, the amount of $ZrSiO_4$ generated increases steadily, correlating with a marked deterioration in the oxidation resistance. In contrast, the samples doped with rare earth oxides exhibit sustained oxidation resistance because the generated rare earth silicates provide superior oxygen resistance.

The surface microstructure and elemental distribution of oxidized ZS20 are shown in Fig. 5a-d. After oxidation, ZS20 was converted into ZrO_2, B_2O_3, and SiO_2, which subsequently reacted at high temperatures to form a protective layer composed of $ZrSiO_4$ and borosilicate glass phases. The oxidized surface of ZS20 is distributed inhomogeneous protuberances and holes, which may be attributed to the volume expansion of oxides and the escape of the low melting point B_2O_3 and CO gases [45,46]. The oxidized surface of ZS20S5 is relatively flat compared with ZS20 (Fig. 5e-g), and the results of EDS mapping and point scanning reveal that the primary component of the glassy phase is SiO_2. The granular phases correspond to ZrO_2, while the surface is coated with B_2O_3. Sc^{3+} is mainly distributed within the ZrO_2 aggregates, and a portion of Sc^{3+} may have dissolved into the ZrO_2 lattice at high temperatures, which induces the formation of t-ZrO_2. This can also be explained by the fact that the oxidized ZS20S5 sample contains a higher content of t-ZrO_2, and the content of t-ZrO_2 is regulated by the solid solution of rare earth elements in the ZrO_2 lattice [47,48]. The volumetric changes during the phase transition result in the formation of protrusions. Furthermore, Sc_2O_3 can react with SiO_2 to form $Sc_2Si_2O_7$ at high temperatures, and the distribution of $Sc_2Si_2O_7$ in B_2O_3 can effectively increase the glass viscosity, thereby reducing the B_2O_3 volatilization [49]. As presented in Fig. 5h-j, the oxidized surface of ZS20Y5 exhibits a uniform distribution of ZrO_2 particles, accompanied by discontinuous borosilicate glass phases, with no obvious glassy protective layer observed. This suggests that Y_2O_3 doping may decrease the fluidity of the glass phase, thereby preventing the formation of a continuous protective film, as corroborated by Fig. 5i, j. As presented in Fig. 5k-m, ZS20L5 exhibits a flatter and denser oxidized surface compared with other samples, with the glass phase primarily composed of B-Si-O-La system. The area uncovered by the glass phase is mainly ZrO_2 particles, and the borosilicate glass phase is uniformly filled between the ZrO_2 particles, which effectively blocks the diffusion of oxygen. This also explains why $Y_2Si_2O_7$ has the highest oxygen adsorption energy compared to $La_2Si_2O_7$, the oxidation resistance of ZS20Y5 is inferior to that of ZS20L5. Oxidation cross-sections in Fig. S7 demonstrate that incorporating rare earth oxides decreases the oxidation layer depth compared to ZS20. Among these samples, ZS20L5 exhibits the densest

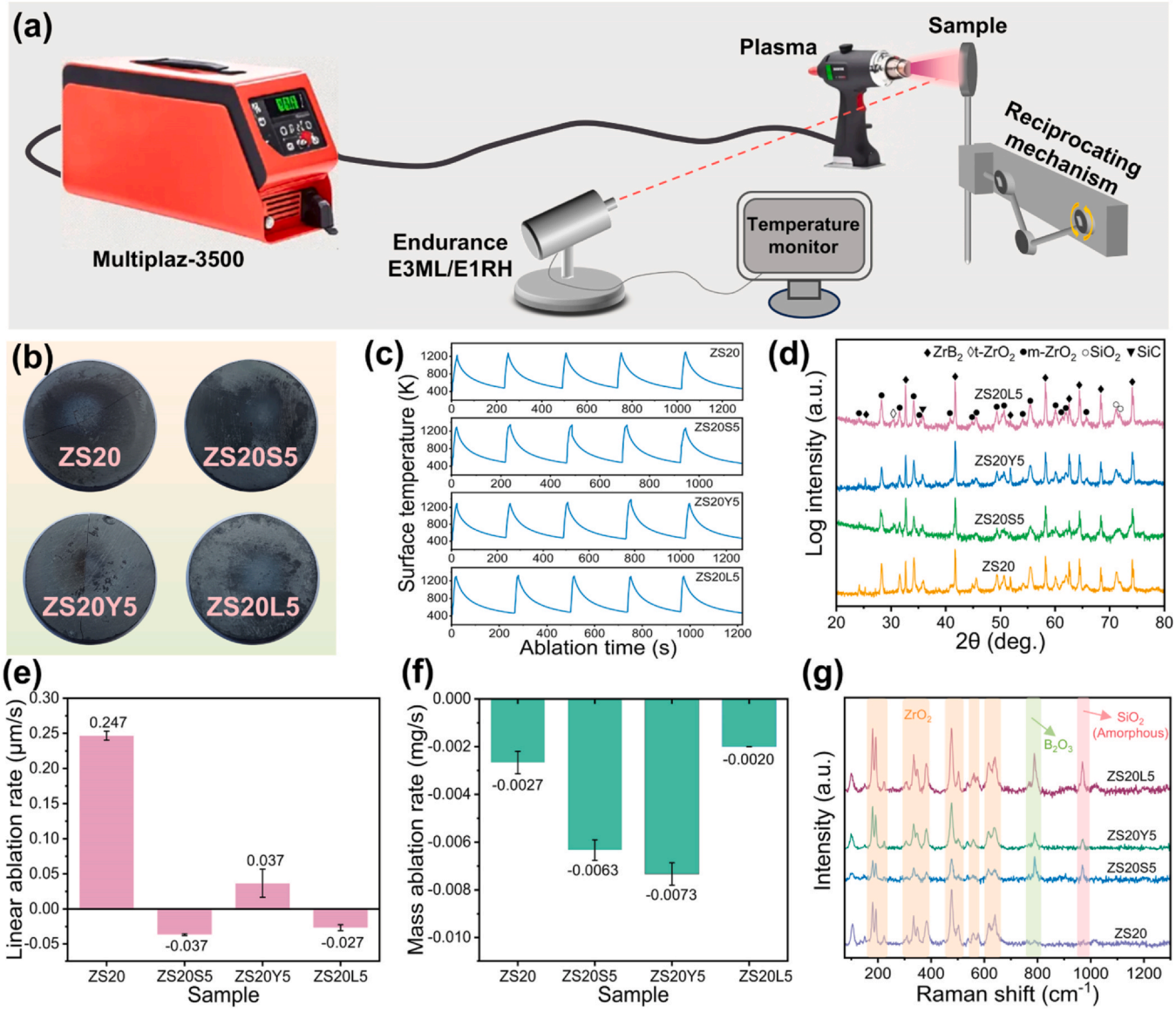

Fig. 6. Ablation tests and performance of the fabricated composites: (a) schematic of the ablation testing setup, (b) macroscopic images of ZS20, ZS20S5, ZS20Y5 and ZS20L5 after ablation, (c) surface temperature evolution profiles during ablation, (d) XRD analysis after ablation test, (e) linear ablation rate of composites, (f) mass ablation rate of composites, (g) Raman spectra of the ablation center.

oxide layer and the shallowest oxidation depth. In summary, the addition of La_2O_3 results in the optimal comprehensive effect of the glass phase, which is most conducive to improving ZrB_2-SiC oxidation resistance.

3.3. Ablation behavior and mechanism of ZrB_2-SiC-based composites

To further evaluate the service performance of the composites under operating conditions, cyclic ablation testing was performed via air plasma flame. The setup of the ablation experiment is shown in Fig. 6a, where the temperature was set at 2273 K, the duration of a single ablation cycle was 20 s, and the experiment was repeated for 5 cycles. Fig. 6b presents the macro images of the four composites after ablation. Specifically, ZS20 cracked after 4 ablation cycles, ZS20Y5 cracked after 5 ablation cycles, while ZS20S5 and ZS20L5 remained intact after the experiment. This indicates that rare earth oxide additions improve the thermal stability of the composites under cyclic ablation conditions. Fig. 6c shows the surface temperature variations of the composites during ablation test, with rapid heating within the first 10 s. Notably, the ZS20, ZS20S5, ZS20Y5, and ZS20L5 samples reached peak temperatures of 1302 K, 1345 K, 1388 K, and 1335 K, respectively. This indicates the possible existence of an effective thermal barrier effect. During ablation, the oxide layer formed on the material surface (such as porous ZrO_2 and silicate glass) typically exhibits a high spectral emissivity (ε) at elevated temperatures. This enables the samples to efficiently re-radiate the heat absorbed via convection and conduction to the surrounding environment. Furthermore, the relatively short duration of single ablation cycle also contributes to the low surface temperature of the composite. The slight increase in the surface temperature of the composites may be attributed to rare earth oxide doping, which inhibits the volatilization of B_2O_3 and SiO_2 [50], thereby reducing heat loss through volatilization and resulting in a slight surface temperature increase.

The XRD analysis (Fig. 6d) reveals that the composite surfaces are primarily consist of ZrB_2 and m-ZrO_2, with trace amounts of SiO_2. As illustrated in Fig. 6e, the incorporation of rare earth oxides leads to a notable reduction in the linear ablation rate. Fig. 6f shows that the mass ablation rate of sample ZS20L5 is close to zero, suggesting minimal mass change. During ablation, the material undergoes oxidation, volatilization, and mechanical erosion concurrently. While oxidation tends

to increase both mass and thickness, volatilization and erosion contribute to their reduction. The mass ablation rate of ZS20 composite is closer to 0 compared with ZS20S5 and ZS20Y5, which may be due to the rapid volatilization or erosion of the oxides generated during the ablation, as supported by the higher linear ablation rate of ZS20 (Fig. 6e). The reason for the difference in ablation rate is that the surface of ZS20 formed an oxide layer mainly composed of ZrO_2 and low-viscosity borosilicate glass phase after ablation. The porous structure exhibits low strength and weak adhesion, making it highly susceptible to erosion under the shear action of high-speed airflow. Consequently, the material undergoes rapid recession in the thickness direction, leading to an extremely high linear ablation rate. However, the relatively low mass ablation rate does not indicate the absence of material loss, but rather the offset between intense oxidation weight gain and severe weight loss from volatilization/erosion. The addition of Y_2O_3 promotes the formation of $Y_2Si_2O_7$ and a glass phase with higher viscosity, which exhibits stronger anchoring to the ZrO_2 framework, resulting in significantly enhanced resistance to mechanical erosion by gas flow compared to ZS20. Consequently, as the oxidation proceeds, most oxidation products are retained on the sample surface, resulting in a more negative mass ablation rate. By comparing the linear ablation and mass ablation rates, ZS20L5 demonstrates superior ablation resistance. The reason why both the linear ablation rate and mass ablation rate of ZS20L5 are close to 0 lies in the possible formation of a glass phase with superior fluidity and oxygen barrier performance, which results in smaller oxidation-induced weight gain and mass change caused by gas flow erosion. Fig. S8 compares the ablation rates of ZS20 and ZS20L5 composites with other typical UHTCs reported in the literature. It can be seen that the ablation resistance of ZS20L5 composites is comparable to that of most UHTCs under the same similar conditions.

Fig. 6g shows the Raman spectra of the ablation center region, where the samples containing rare earth oxides display more intense Raman peaks corresponding to B_2O_3 and SiO_2 [51,52]. This implies that the addition of rare earth oxides effectively inhibits the glass phase volatilization during ablation, thereby improving the ablation resistance.

The micrographs and elemental maps of ZS20 ablation center are displayed in Fig. 7a-d. The microstructure reveals a porous surface characterized by a ZrO_2-wrapped borosilicate glass skeleton, abundant with holes and bubbles. This morphology primarily results from the high-temperature liberation of low melting point B_2O_3 and gaseous CO/CO_2 products from the oxide layer. Fig. 7e-h shows the microstructure of ZS20S5 ablation center reveals a significant amount of plate like glass phases, with the main component being the B-Si-O-Sc system. The areas uncovered by the glassy phase are primarily aggregated ZrO_2 particles, with some cracks visible on the surface. Fig. 7i-l shows the microstructure of ZS20Y5 ablation center. Similar to ZS20S5, the ablation center of ZS20Y5 also contains a significant amount of plate like glass phases, whose main component is the B-Si-O-Y system. However, the ablated surface of ZS20Y5 exhibits more cracks, and no obvious glass phase is observed between the cracks. Fig. 7m-p shows the microstructure of ZS20L5 ablation center. Only a small amount of plate like glass phase exists in the ablation center of ZS20L5, with B_2O_3 as the main component. The ablated surface of ZS20L5 has few cracks, and these cracks are well filled with glass phase. In summary, the glass phase formed at high temperatures of samples doped with Sc_2O_3 and Y_2O_3 exhibit inferior fluidity, which promotes the rapid formation of the glass phase during the ablation, leading to the crack formation due to the volume shrinkage of ZrO_2. The absence of glass phase filling allows the cracks become the diffusion channel for oxygen. The glass phase formed in the La_2O_3-doped sample exhibits superior fluidity at high temperatures, which can

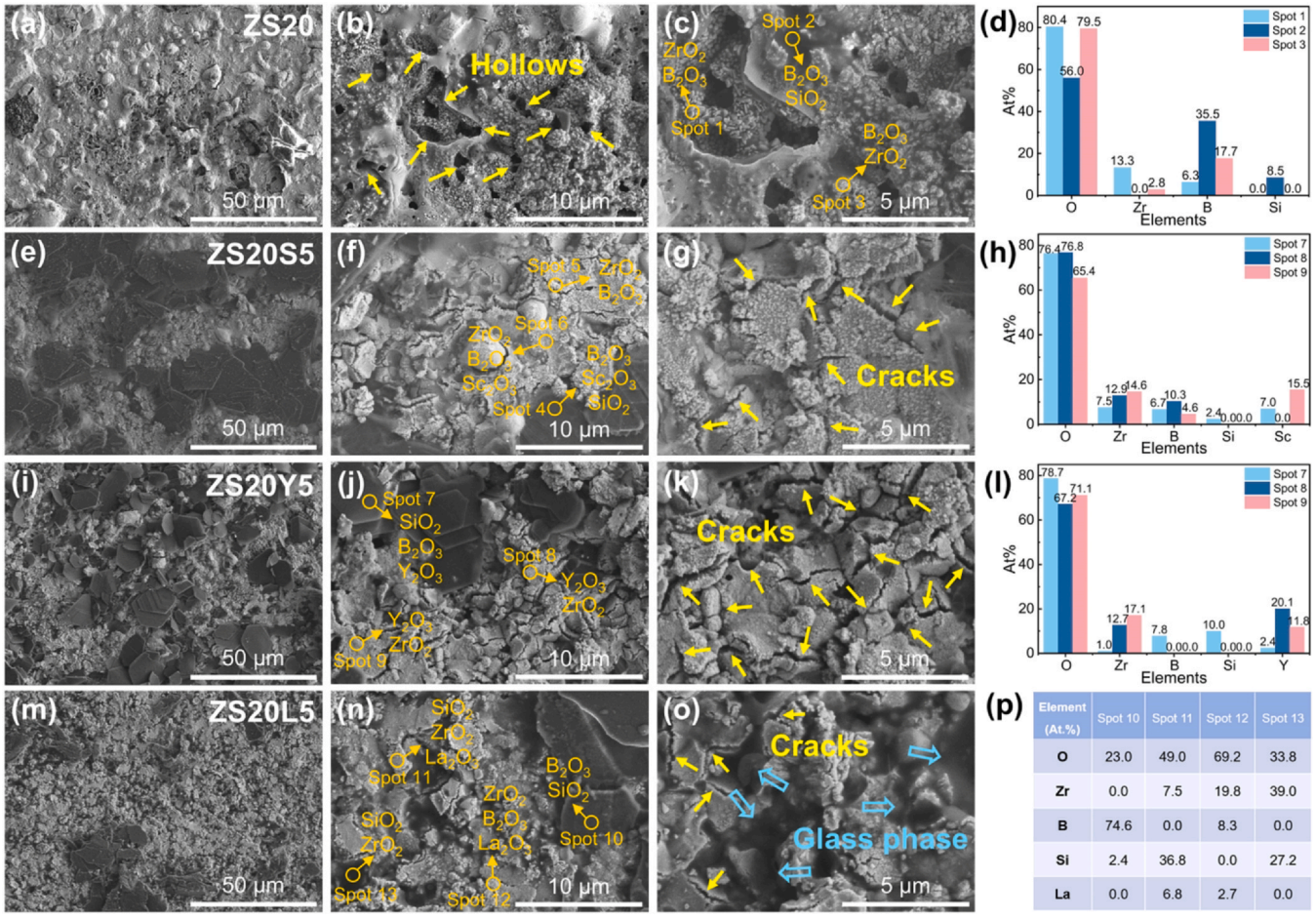

Element (At.%)	Spot 10	Spot 11	Spot 12	Spot 13
O	23.0	49.0	69.2	33.8
Zr	0.0	7.5	19.8	39.0
B	74.6	0.0	8.3	0.0
Si	2.4	36.8	0.0	27.2
La	0.0	6.8	2.7	0.0

Fig. 7. Microstructure and compositional analysis of the composites surface after ablation test: (a-d) ZS20, (e-h) ZS20S5, (i-l) ZS20Y5, (m-p) ZS20L5.

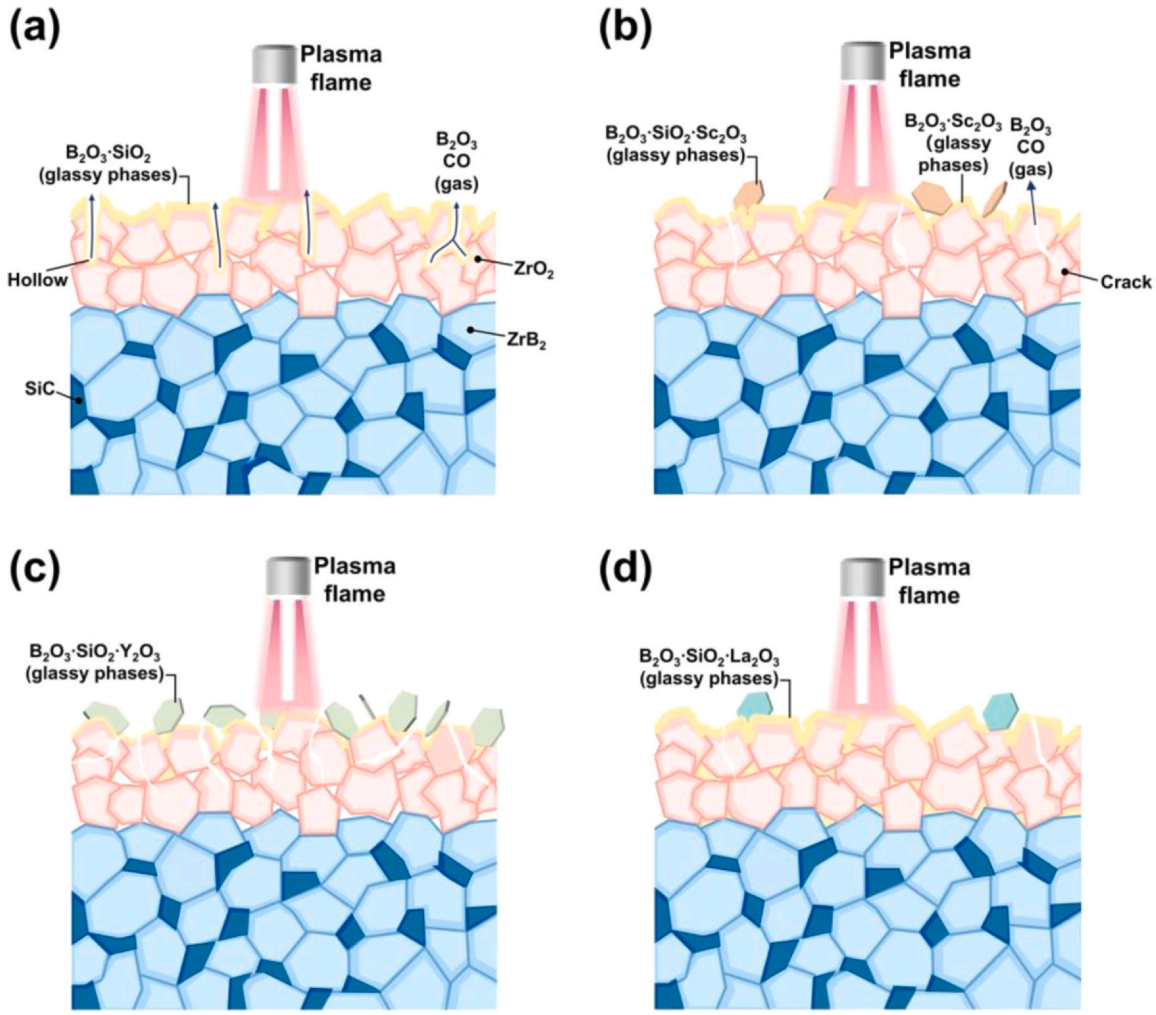

Fig. 8. Schematic of the ablation mechanism of the samples: (a) ZS20, (b) ZS20S5, (c) ZS20Y5, (d) ZS20L5.

effectively fill the cracks, seal pores, improve the density of the oxide film, and block the diffusion of oxygen [53].

Fig. 8 demonstrates the schematic diagram of the ablation mechanism across four specimens. At high temperature aerobic environment, the composites undergo oxidization to form B_2O_3, SiO_2, and ZrO_2. However, the holes left by the volatilization of B_2O_3 and gases, along with the consumption of SiO_2, result in a degradation of the ablation performance. The ZS20S5 and ZS20Y5 exhibit better ablation resistance compared to ZS20, which is attributed to the formation of plate like glass phase on the surface that provides a more effective oxygen blocking effect. Nevertheless, the cracks present on the surface still act as diffusion channels for oxygen. In contrast, ZS20L5 exhibits superior ablation performance due to the enhanced flowability of its high-temperature glass phase, which forms a dense, stable and continuous protective barrier, effectively inhibiting oxygen diffusion.

4. Conclusions

In this study, ZrB_2-SiC composites doped with 5 vol% rare earth oxides (Sc_2O_3, Y_2O_3, La_2O_3) were fabricated by hot press sintering. Subsequently, the behavior differences and mechanisms of these composites under static oxidation at 1773 K and cyclic ablation in an air plasma environment at the middle-low temperature zones were comparatively investigated. The principal conclusions are as follows:

(1) Rare earth oxides as sintering additives slightly enhance the densification of ZrB_2-SiC composites. Benefiting from the increased in density, the mechanical performance of the composites is slightly improved by the inclusion of rare earth oxides.
(2) Rare earth oxides additives effectively improve the oxidation resistance of ZrB_2-SiC composites at 1773 K. Specifically, the ZS20L5 sample demonstrates the lowest weight gain and oxidation rate constant during oxidation, with a post-oxidation porosity of only 1.8 %, indicating its optimal long-term oxidation resistance.
(3) Theoretical calculations and thermodynamic analyses reveal that the excellent oxidation resistance of the composites doped with rare earth oxide stems from the preferential reaction between rare earth oxides and SiO_2 to form rare earth silicates with superior oxygen-blocking capabilities, thereby preventing the formation of $ZrSiO_4$, which is less effective at oxygen blocking.
(4) Cyclic ablation testing at the middle-low temperature zones revealed that ZS20L5 maintained structural integrity through 5 cycles and exhibited the lowest ablation rates. The superior ablation resistance originates from the development of a continuous, highly fluid vitreous layer at elevated temperatures, which can promptly fill cracks, seal volatile pores, and block oxygen diffusion. In comparison, samples containing Sc_2O_3 and Y_2O_3 tend to form plate like glass phases, which have less effective oxygen blocking performance.

CRediT authorship contribution statement

Zhulin Huang: Writing – review & editing, Validation, Supervision, Resources, Funding acquisition, Conceptualization. **Xian Dang:**

Software, Data curation. **Guowen Meng:** Writing – review & editing, Resources. **Chengwan Yang:** Formal analysis. **Kewei Li:** Writing – review & editing. **Hanwen Zhang:** Investigation. **Zhen Wang:** Funding acquisition. **Shuxin Li:** Supervision. **Yuebin Li:** Writing – review & editing. **Xiaoye Hu:** Supervision, Resources. **Yue Li:** Writing – review & editing, Supervision. **Abdumutolib Atakhanov:** Writing – review & editing, Formal analysis. **Mengen Hu:** Writing – original draft, Investigation, Data curation.

Declaration of Competing Interest

The authors declare that they have no known competing financial interests or personal relationships that could have appeared to influence the work reported in this paper.

Acknowledgements

This work was financially supported by the Natural Science Fund for Excellent Young Scholars (Grant No. 52222208), the Key Science & Technology Project of Anhui Province (202423i08050053), and the China Postdoctoral Science Foundation (Grant No. 2025M770147).

Appendix A. Supporting information

Supplementary data associated with this article can be found in the online version at doi:10.1016/j.exm.2025.12.001.

References

[1] Z.H. Wen, Y.W. Liu, J. Yang, Y.H. Chen, Y.M. Fu, L. Zhuang, H.L. Yu, Y.H. Chu, Exceptional oxidation resistance of high-entropy carbides up to 3600 °C, Adv. Mater. (2025) 2507254, https://doi.org/10.1002/adma.202507254.

[2] Y.R. Lin, T. Koyanagi, D.J. Sprouster, C.M. Petrie, W. Fahrenholtz, G.E. Hilmas, Y. Katoh, Response of ^{11}B enriched ZrB_2 ultra-high temperature ceramic to neutron irradiation at elevated temperatures, Acta Mater. 276 (2024) 120111, https://doi.org/10.1016/j.actamat.2024.120111.

[3] C. Fang, S. Dong, X.H. Zhang, Y.C. Zhou, Breaking the 3000 °C melting temperature barrier of oxide ceramics, J. Adv. Ceram. (2025), https://doi.org/10.26599/JAC.2025.9221193.

[4] B.R. Golla, A. Mukhopadhyay, B. Basu, S.K. Thimmappa, Review on ultra-high temperature boride ceramics, Prog. Mater. Sci. 111 (2020) 100651, https://doi.org/10.1016/j.pmatsci.2020.100651.

[5] Q.Y. Deng, P.F. He, C. Sun, Y. Li, Y. Xing, Y.J. Wang, J.L. Li, X.B. Liang, X. Wang, Y.J. Zhou, Y.J. Cai, High speed laser cladding as a new approach to prepare ultra-high temperature ceramic coatings, J. Adv. Ceram. 13 (2024) 143–154, https://doi.org/10.26599/jac.2024.9220827.

[6] D.W. Ni, Y. Cheng, J.P. Zhang, J.X. Liu, J. Zou, B.W. Chen, H.Y. Wu, H.J. Li, S.M. Dong, J.C. Han, X.H. Zhang, Q.G. Fu, G.J. Zhang, Advances in ultra-high temperature ceramics, composites, and coatings, J. Adv. Ceram. 11 (2022) 1–56, https://doi.org/10.1007/s40145-021-0550-6.

[7] N.P. Padture, Advanced structural ceramics in aerospace propulsion, Nat. Mater. 15 (2016) 804–809, https://doi.org/10.1038/nmat4687.

[8] K.W. Li, Z.L. Huang, J.Y. Yuan, X.Y. Li, Z. Wang, M.E. Hu, T.X. Wang, X.Y. Hu, Y. Li, X.H. Zhang, Synthesis and growth mechanism of highly crystalized multi-branched HfB_2 microrods with self-toughening effect, Mater. Des. 244 (2024) 113196, https://doi.org/10.1016/j.matdes.2024.113196.

[9] X. Dang, Z.L. Huang, J.Y. Yuan, K. Li, M.G. Hu, Z.M. Xie, H.R. Song, B.S. Chen, X.Y. Li, M. Li, X.Y. Hu, Y. Li, Improved spectral emissivity and mechanical properties of high-entropy $(Ti_{0.2}Zr_{0.2}Nb_{0.2}Mo_{0.2}Hf_{0.2})B_2$ derived from boro/carbothermal reduction, J. Eur. Ceram. Soc. 44 (2024) 4410–4424, https://doi.org/10.1016/j.jeurceramsoc.2024.01.091.

[10] R. Naraparaju, K. Maniya, A. Murchie, W.G. Fahrenholtz, G.E. Hilmas, Effect of moisture on the oxidation behavior of ZrB_2, J. Am. Ceram. Soc. 104 (2021) 1058–1066, https://doi.org/10.1111/jace.17500.

[11] B.C. Wyatt, S.K. Nemani, G.E. Hilmas, E.J. Opila, B. Anasori, Ultra-high temperature ceramics for extreme environments, Nat. Rev. Mater. 9 (2024) 773–789, https://doi.org/10.1038/s41578-023-00619-0.

[12] Z. Wang, Y. Cheng, K.W. Li, M.G. Hu, H.W. Zhang, X. Dang, M. Li, X.Y. Li, Z.L. Huang, Y. Li, X.Y. Hu, Growth mechanism and sintering properties of high crystallinity Archimedean polyhedral $(Zr_{0.5}Hf_{0.5})B_2$ nanoparticles, J. Eur. Ceram. Soc. 45 (2025) 117251, https://doi.org/10.1016/j.jeurceramsoc.2025.117251.

[13] Z.Y. Tang, Z.H. Wen, L. Zhuang, H.L. Yu, Y.H. Chu, Enhanced oxidation resistance of high-entropy diborides by multi-component synergistic effects, Sci. China Mater. 67 (2024) 3392–3400, https://doi.org/10.1007/s40843-024-3045-4.

[14] F.C. Liu, B.W. Chen, D.W. Ni, Q. Wang, F.Y. Cai, C.J. Liao, H.D. Wang, Y.S. Ding, S.M. Dong, Cyclic ablation mechanisms of the YB_4-$CrSi_2$ surface-modified Cf/ZrB_2-SiC composites at 2600 °C, Corros. Sci. 255 (2025) 113091, https://doi.org/10.1016/j.corsci.2025.113091.

[15] L.Y. Yang, S. Dong, T.Y. Cui, J.Q. Xin, G.Q. Chen, C.Q. Hong, X.H. Zhang, Novel gradient ZrB_2-$MoSi_2$-SiC dense layer with enhanced emissivity and long-term oxidation resistance at ultra-high temperatures, Rare Met 44 (2025) 2043–2058, https://doi.org/10.1007/s12598-024-02959-4.

[16] C. Young, C. Zhang, A. Loganathan, P. Nautiyal, B. Boesl, A. Agarwal, Densification and oxidation behavior of spark plasma sintered Hafnium Diboride-Hafnium Carbide composite, Ceram. Int. 46 (2020) 14625–14631, https://doi.org/10.1016/j.ceramint.2020.02.263.

[17] T.A. Parthasarathy, R.A. Rapp, M. Opeka, R.J. Kerans, Effects of phase change and oxygen permeability in oxide scales on oxidation kinetics of ZrB_2 and HfB_2, J. Am. Ceram. Soc. 92 (2009) 1079–1086, https://doi.org/10.1111/j.1551-2916.2009.03031.x.

[18] S.B. Sun, H.B. Wang, X.M. Liu, C. Liu, H. Lu, Z.R. Nie, X.Y. Song, Outstanding anti-oxidation performance of boride coating under high-temperature friction, Corros. Sci. 179 (2021) 109133, https://doi.org/10.1016/j.corsci.2020.109133.

[19] M.M. Chen, X.Y. Yao, G.H. Feng, Y. Guo, Anti-ablation performance of La_2O_3-modified ZrB_2 coating on SiC-coated carbon/carbon composites, Ceram. Int. 46 (2020) 28758–28766, https://doi.org/10.1016/j.ceramint.2020.08.038.

[20] S.K. Thimmappa, B.R. Golla, V.V.B. Prasad, oxidation behavior of silicon-based ceramics reinforced diboride UHTC: a review, Silicon 14 (2022) 12049–12074, https://doi.org/10.1007/s12633-022-01945-8.

[21] S.J. Sun, Z. Ma, Y.B. Liu, L. Liu, F.C. Wang, X.T. Luan, Ablation mechanism and properties of SiO_2 modified ZrB_2-SiC coatings fabricated on C/C composites via plasma spraying technology, Surf. Coat. Technol. 381 (2020) 125132, https://doi.org/10.1016/j.surfcoat.2019.125132.

[22] Y.X. Liu, H. Wang, J.C. Hao, Y.H. Cheng, S. Dong, P. Hu, W.B. Han, X.H. Zhang, Key materials for extreme high-temperature environments: Ultra-high-temperature ceramics and their composites, Extrem. Mater. 1 (2025) 38–66, https://doi.org/10.1016/j.exm.2025.01.001.

[23] J. Binner, M. Porter, B. Baker, J. Zou, V. Venkatachalam, V.R. Diaz, A. D'Angio, P. Ramanujam, T.L. Zhang, T. Murthy, Selection, processing, properties and applications of ultra-high temperature ceramic matrix composites, UHTCMCs-a review, Int. Mater. Rev. 65 (2020) 389–444, https://doi.org/10.1080/09506608.2019.1652006.

[24] X.R. Ren, H.L. Shi, W.H. Wang, H.A. Chu, P. Chen, P.Z. Feng, L.T. Guo, Z.Y. Li, Influence of the ZrB_2 content on the anti-oxidation ability of ZrB_2-SiC coatings in aerobic environments with broad temperature range, J. Eur. Ceram. Soc. 40 (2020) 203–211, https://doi.org/10.1016/j.jeurceramsoc.2019.10.006.

[25] Z. Kovácová, L. Orovcík, J. Sedlácek, L. Baca, E. Dobrocka, M. Kitzmantel, E. Neubauer, The effect of YB_4 addition in ZrB_2-SiC composites on the mechanical properties and oxidation performance tested up to 2000 °C, J. Eur. Ceram. Soc. 40 (2020) 3829–3843, https://doi.org/10.1016/j.jeurceramsoc.2020.03.060.

[26] H. Yang, H.S. Zhao, T.W. Wang, X.X. Liu, K.H. Zhang, Z.Q. Li, Y. Gao, B. Liu, A multi-layered SiC coating to protect graphite spheres from high temperature oxidation in static air, Corros. Sci. 183 (2021) 109325, https://doi.org/10.1016/j.corsci.2021.109325.

[27] Y. Lyu, B.H. Du, G.Q. Chen, G.D. Zhao, Y. Cheng, S.B. Zhou, Q.R. Lv, X.H. Zhang, W.B. Han, Microstructural regulation, oxidation resistance, and mechanical properties of Cf/SiC/SiHfBOC composites prepared by chemical vapor infiltration with precursor infiltration pyrolysis, J. Adv. Ceram. 11 (2022) 120–135, https://doi.org/10.1007/s40145-021-0521-y.

[28] J.S. Lv, W. Li, T. Li, B. Gao, J.C. Li, Y.Q. Fu, L.X. Guo, Y.L. Zhang, Multicomponent (Hf-Zr-Ta)B_2 coatings for carbon/carbon composites and structural optimization enabling superior ablation resistance, J. Mater. Sci. Technol. 204 (2025) 115–126, https://doi.org/10.1016/j.jmst.2024.03.050.

[29] X.R. Ren, P.P. Wang, Y.X. Chen, W. Xie, X. Ji, Z.C. Shang, C.S. Ji, J. Zhao, H.Q. Liu, G.Z. Lv, P.Z. Feng, Advances in ultra-high-temperature ceramic coatings with enhanced oxidation resistance for carbon-based composites, Extrem. Mater. 1 (2025) 9–43, https://doi.org/10.1016/j.exm.2025.07.003.

[30] B.W. Chen, D.W. Ni, W.C. Bao, C.J. Liao, W. Luo, E.R. Song, S.M. Dong, Engineering Cf/ZrB_2-SiC-Y_2O_3 for thermal structures of hypersonic vehicles with excellent long-term ultrahigh temperature ablation resistance, Adv. Sci. 10 (2023) 2304254, https://doi.org/10.1002/advs.202304254.

[31] L. Silvestroni, H.T. Liu, D. Sciti, X.G. Wang, G.J. Zhang, Rare earth-doped ZrB_2-$MoSi_2$ ceramics: Densification and oxidation behavior, J. Eur. Ceram. Soc. 45 (2025) 116992, https://doi.org/10.1016/j.jeurceramsoc.2024.116992.

[32] H. Lin, Y.Y. Liu, W.P. Liang, Q. Miao, S.Y. Zhou, J.Y. Sun, Y. Qi, X.G. Gao, Y.D. Song, K. Ogawa, Effect of the Y_2O_3 amount on the oxidation behavior of ZrB_2-SiC-based coatings for carbon/carbon composites, J. Eur. Ceram. Soc. 42 (2022) 4770–4782, https://doi.org/10.1016/j.jeurceramsoc.2022.05.006.

[33] M.G. Hu, L. Liu, Z. Wang, X. Dang, C.W. Yang, X.Y. Li, M. Li, X.Y. Hu, Y. Li, Z.L. Huang, X.H. Zhang, La_2O_3 stabilized WB_2-SiC composites with remarkable ablation resistance up to 2273, K. J. Eur. Ceram. Soc. 45 (2025) 117298, https://doi.org/10.1016/j.jeurceramsoc.2025.117298.

[34] D.Y. Qian, Y.X. Chen, X.R. Ren, L.Y. Wang, J.P. Chen, Y. Zhao, D.L. Shi, Y. Li, H.B. Du, P.Z. Feng, Effect of La_2O_3 content on the oxygen barrier ability of the HfB_2-SiC coating at 1973 K, J. Am. Ceram. Soc. 106 (2023) 2155–2168, https://doi.org/10.1111/jace.18876.

[35] B. Liu, J. Sun, L.X. Guo, H.L. Shi, G.H. Feng, L. Feldmann, X.M. Yin, R. Riedel, Q.G. Fu, H.J. Li, Materials design of silicon based ceramic coatings for high temperature oxidation protection, Mater. Sci. Eng. R. 163 (2025) 100936, https://doi.org/10.1016/j.mser.2025.100936.

[36] H.C. Ma, Q. Miao, W.P. Liang, Y.Y. Liu, H. Lin, H.R. Ma, S.W. Zuo, L. Xue, High temperature oxidation resistance of Y_2O_3 modified ZrB_2-SiC coating for carbon/carbon composites, Ceram. Int. 47 (2021) 6728–6735, https://doi.org/10.1016/j.ceramint.2020.11.015.
[37] S. Stemmer, Thermodynamic considerations in the stability of binary oxides for alternative gate dielectrics in complementary metal-oxide-semiconductors, J. Vac. Sci. Technol. B 22 (2004) 791–800, https://doi.org/10.1116/1.1688357.
[38] M.E. Hu, Z.L. Huang, X.Y. Li, Y. Cheng, Z. Wang, K.W. Li, T.X. Wang, X.Y. Hu, Y. Li, X.H. Zhang, Ultrafine ZrB_2 Ceramic Powders Prepared by a Sol–Gel Method Synergized with a Carbothermic Reaction and Their Improved Sintering Performance, ACS Appl. Eng. Mater. 1 (2023) 769–779, https://doi.org/10.1021/acsaenm.2c00195.
[39] A. Vinci, L. Zoli, P. Galizia, D. Sciti, Influence of Y_2O_3 addition on the mechanical and oxidation behaviour of carbon fibre reinforced ZrB_2/SiC composites, J. Eur. Ceram. Soc. 40 (2020) 5067–5075, https://doi.org/10.1016/j.jeurceramsoc.2020.06.043.
[40] D.H. Muksin, K. Yoon, Raju, Effects of Sc_2O_3 sintering aid for the densification and mechanical properties of SiC-ZrB_2 composites, Ceram. Int. 42 (2016) 7300–7308, https://doi.org/10.1016/j.ceramint.2016.01.126.
[41] W. Xu, L. Shi, Y.H. Zheng, Transient analysis of nuclear graphite oxidation for high temperature gas Cooled reactor, Nucl. Eng. Des. 306 (2016) 138–144, https://doi.org/10.1016/j.nucengdes.2016.04.029.
[42] Z.H. Wen, Z.Y. Tang, H. Meng, Y.H. Chu, A promising new class of high-entropy ceramics: High-entropy oxycarbides with good oxidation resistance, Corros. Sci. 207 (2022) 110574, https://doi.org/10.1016/j.corsci.2022.110574.
[43] Z.H. Wen, Z.Y. Tang, H. Meng, L. Zhuang, H.L. Yu, Y.H. Chu, Ultrafast synthesis of high-entropy carbides up to 3,273 K for superior oxidation resistance, Cell Rep. Phys. Sci. 5 (2024) 101821, https://doi.org/10.1016/j.xcrp.2024.101821.
[44] Y.Q. Li, T. Qiu, Oxidation behaviour of boron carbide powder, Mater. Sci. Eng. A 444 (2007) 184–191, https://doi.org/10.1016/j.msea.2006.08.068.
[45] W.N. Tan, M. Adducci, R. Trice, Evaluation of Rare-Earth Modified ZrB_2-SiC Ablation Resistance Using an Oxyacetylene Torch, J. Am. Ceram. Soc. 97 (2014) 2639–2645, https://doi.org/10.1111/jace.12991.
[46] T.A. Parthasarathy, R.A. Rapp, M. Opeka, M.K. Cinibulk, Modeling Oxidation Kinetics of SiC-Containing Refractory Diborides, J. Am. Ceram. Soc. 95 (2012) 338–349, https://doi.org/10.1111/j.1551-2916.2011.04927.x.
[47] J. Zhou, C.X. Ren, C.L. Tian, M. Omran, J. Tang, F. Zhang, G. Chen, The phase-stabilized behavior of Sc_2O_3-Y_2O_3 co-doped ZrO_2 nanopowders by co-precipitation synthesis, Ceram. Int. 50 (2024) 24823–24834, https://doi.org/10.1016/j.ceramint.2024.04.218.
[48] H. Jeon, I. Lee, Y. Oh, Changes in high-temperature thermal properties of modified YSZ with various rare earth doping elements, Ceram. Int. 48 (2022) 8177–8185, https://doi.org/10.1016/j.ceramint.2021.12.020.
[49] Z.T. Tabari, S.Z. Heris, Heat Transfer Performance of Milk Pasteurization Plate Heat Exchangers Using MWCNT/Water Nanofluid, J. Dispers. Sci. Technol. 36 (2015) 196–204, https://doi.org/10.1080/01932691.2014.894917.
[50] W. Xie, Q.G. Fu, C.Y. Cheng, N.N. Yan, Experimental and theoretical study on the effect of different rare-earth oxides on the high-temperature stability of SiO_2 glass at 1973K, Ceram. Int. 46 (2020) 24371–24378, https://doi.org/10.1016/j.ceramint.2020.06.219.
[51] M. Chromcíková, A.A. Osipov, L.M. Osipova, B. Hruska, J. Michálková, A. Nowicka, J.A. Peterson, M. Liska, Thermodynamic model and Raman spectra of binary barium borate glassforming melts, J. Therm. Anal. Calor. 142 (2020) 945–951, https://doi.org/10.1007/s10973-020-09329-z.
[52] Y.X. Zhang, H.R. Li, S.Y. Liu, N.N. Wu, S.L. OuYang, Raman spectroscopic study of irregular network in the process of glass conversion to CaO-MgO-Al_2O_3-SiO_2 glass-ceramics, J. NonCryst. Solids 563 (2021) 120701, https://doi.org/10.1016/j.jnoncrysol.2021.120701.
[53] D.Y. Qian, Y.X. Chen, X.R. Ren, L.Y. Wang, J.P. Chen, Y. Zhao, D.L. Shi, Y. Li, H.B. Du, P.Z. Feng, Effect of La_2O_3 content on the oxygen barrier ability of the HfB_2-SiC coating at 1973 K, J. Am. Ceram. Soc. 106 (2023) 2155–2168, https://doi.org/10.1111/jace.18876.